

See discussions, stats, and author profiles for this publication at: <https://www.researchgate.net/publication/320256909>

Reconstruction of Missing Imagery Data Caused by Cloudcover Based on Bayesian Neural Network and Multitemporal Images

Conference Paper · October 2018

DOI: 10.1007/978-3-319-68240-2_6

CITATIONS

0

READS

234

2 authors, including:



Hien Phu La

Hanoi University of Mining and Geology

22 PUBLICATIONS 67 CITATIONS

[SEE PROFILE](#)

Some of the authors of this publication are also working on these related projects:



2012 project [View project](#)

Dieu Tien Bui · Anh Ngoc Do
Hoang-Bac Bui · Nhat-Duc Hoang
Editors

Advances and Applications in Geospatial Technology and Earth Resources

Proceedings of the International
Conference on Geo-Spatial Technologies
and Earth Resources 2017

Contents

A Computational Tool for Time-Series Prediction of Mining-Induced Subsidence Based on Time-Effect Function and Geodetic Monitoring Data	1
Nguyen Quoc Long, Xuan-Nam Bui, Luyen Khac Bui, Khoa Dat Vu Huynh, Canh Van Le, Michał Buczek, and Thang Phi Nguyen	
Lightweight Unmanned Aerial Vehicle and Structure-from-Motion Photogrammetry for Generating Digital Surface Model for Open-Pit Coal Mine Area and Its Accuracy Assessment	17
Dieu Tien Bui, Nguyen Quoc Long, Xuan-Nam Bui, Viet-Nghia Nguyen, Chung Van Pham, Canh Van Le, Phuong-Thao Thi Ngo, Dung Tien Bui, and Bjørn Kristoffersen	
Energy Analysis in Semiautomatic and Automatic Velocity Estimation for Ground Penetrating Radar Data in Urban Areas: Case Study in Ho Chi Minh City, Vietnam	34
Thuan Van Nguyen, Cuong Anh Van Le, Van Thanh Nguyen, Trung Hoai Dang, Triet Minh Vo, and Lieu Nguyen Nhu Vo	
An Integration of Least Squares Support Vector Machines and Firefly Optimization Algorithm for Flood Susceptible Modeling Using GIS . . .	52
Viet-Nghia Nguyen, Dieu Tien Bui, Phuong-Thao Thi Ngo, Quoc-Phi Nguyen, Van Cam Nguyen, Nguyen Quoc Long, and Inge Revhaug	
Estimation of Surface Parameters of Tidal Flats Using Sentinel-1A SAR Data in the Northern Coast of Vietnam	65
Si Son Tong, Jean Paul Deroin, Thi Lan Pham, and Xuan Cuong Cao	
Reconstruction of Missing Imagery Data Caused by Cloudcover Based on Bayesian Neural Network and Multitemporal Images	89
Hien Phu La and Minh Quang Nguyen	

Monitoring Mangrove Forest Changes in Cat Ba Biosphere Reserve Using ALOS PALSAR Imagery and a GIS-Based Support Vector Machine Algorithm	103
Tien Dat Pham, Kunihiro Yoshino, and Naoko Kaida	
Detection and Prediction of Urban Expansion of Hanoi Area (Vietnam) Using SPOT-5 Satellite Imagery and Markov Chain Model	119
Trung Van Nguyen, Nam Van Nguyen, Ha Thu Thi Le, Hien Phu La, and Dieu Tien Bui	
Analysis of Land Cover Changes in Northern Vietnam Using High Resolution Remote Sensing Data	134
Thanh Tung Hoang, Kenlo Nishida Nasahara, and Jin Katagi	
Change Detection in Multitemporal SAR Images Using a Strategy of Multistage Analysis	152
Thu Trang Lê, Van Anh Tran, Ha Thai Pham, and Xuan Truong Tran	
Understanding Factors Affecting the Outbreak of Malaria Using Locally-Compensated Ridge Geographically Weighted Regression: Case Study in DakNong, Vietnam	166
Tuan-Anh Hoang, Le Hoang Son, Quang-Thanh Bui, and Quoc-Huy Nguyen	
A Novel Hybrid Model of Rotation Forest Based Functional Trees for Landslide Susceptibility Mapping: A Case Study at Kon Tum Province, Vietnam	186
Binh Thai Pham, Viet-Tien Nguyen, Van-Liem Ngo, Phan Trong Trinh, Huong Thanh Thi Ngo, and Dieu Tien Bui	
Effects of Residual Soil Characteristics on Rainfall-Induced Shallow Landslides Along Transport Arteries in Bac Kan Province, Vietnam . . .	202
Do Minh Duc, Dao Minh Duc, and Do Minh Ngoc	
Spatial Prediction of Rainfall Induced Shallow Landslides Using Adaptive-Network-Based Fuzzy Inference System and Particle Swarm Optimization: A Case Study at the Uttarakhand Area, India	224
Binh Thai Pham and Indra Prakash	
GIS-Based Landslide Spatial Modeling Using Batch-Training Back-propagation Artificial Neural Network: A Study of Model Parameters	239
Nhat-Duc Hoang and Dieu Tien Bui	

A Novel Hybrid Intelligent Approach of Random Subspace Ensemble and Reduced Error Pruning Trees for Landslide Susceptibility Modeling: A Case Study at Mu Cang Chai District, Yen Bai Province, Viet Nam	255
Binh Thai Pham and Indra Prakash	
Recent Tectonic Movements Along the Coastal Zone of Tuy Hoa Area (Central Vietnam) and Its Significance for Coastal Hazards in the Case of Sea Level Rise	270
Hai Thanh Tran	
Isotopic and Hydrogeochemical Signatures in Evaluating Groundwater Quality in the Coastal Area of the Mekong Delta, Vietnam	293
Tran Dang An, Maki Tsujimura, Vo Le Phu, Doan Thu Ha, and Nguyen Van Hai	
Research Progress on Stabilization/Solidification Technique for Remediation of Heavy Metals Contaminated Soil	315
Yu Zhang, Cong Lu, Mengyi Xu, Lingling Pan, Nguyen Chau Lan, and Qiang Tang	
Distribution and Reserve Potential of Titanium-Zirconium Heavy Minerals in Quang an Area, Thua Thien Hue Province, Vietnam	326
Nguyen Tien Dung, Bui Hoang Bac, Do Manh An, and Tran Thi Van Anh	
Application of Land Subsidence Inversion for Salt Mining-Induced Rock Mass Movement	340
Ryszard Hejmanowski and Agnieszka A. Malinowska	
Study on the Coupling Effect Between Surrounding Rock and Support Structures of Tunnels	355
Pham Thi Nhan, Guangsheng Zhang, Viet-Nghia Nguyen, and Viet Huy Le	
Numerical Simulation of CFRA Pile Subgrade Reinforcement Based on Recycled Aggregate of Demolition Waste	367
Huanda Gu, Cong Lu, Guoqiang Xue, Huilong Wu, Nguyen Chau Lan, and Qiang Tang	
Worthiness Assessment of New Mining Projects: The Case of Potash Mining in Bamnet Narong, Thailand	378
Kridtaya Sakamornsnguan and Jürgen Kretschmann	
Author Index	395

Reconstruction of Missing Imagery Data Caused by Cloudcover Based on Bayesian Neural Network and Multitemporal Images

Hien Phu La^(✉) and Minh Quang Nguyen

Faculty of Geomatics and Land Administration,
Hanoi University of Mining and Geology, Hanoi, Vietnam
hien.phu.la@gmail.com

Abstract. One of passive sensor's limitations is its high sensitivity to weather condition during image acquiring process. Consequently, the image is often affected by cloud cover. This phenomenon severely influences the completeness of land use/cover obtained from optical satellite imagery and make image processing more complicatedly. However, the pattern of pixel values based on the season and weather changes determined from substantial remote sensing data within a region can help to reconstruct the imagery data which was missed due to the presence of clouds. Taking advantage of datasets containing a substantial amount of multitemporal images, this study proposed a method to reconstruct missed imagery data caused by cloud cover based on relationship between air temperature, humidity, visibility, rainfall, normalized difference vegetation index, direct solar radiation, diffuse solar radiation, reflected radiation and spectral radiance of each pixel obtained by Bayesian Neural Network. The proposed method was applied to generate a cloud-free Landsat image. The results showed that pixels generated by the proposed algorithm are very similar to the actual pixels, especially in non-change area with percentage of correlation coefficients (R) over 0.99 is approximate to 91%. However, the similarity reduced in areas which changed significantly over time period, with the percentages of R over 0.99 are about 78%.

Keywords: Bayesian neural network · Cloud-free image generation · Landsat image

1 Introduction

One disadvantage of a passive remote-sensing and optical sensor is its high sensitivity to weather conditions during data acquiring process. That means the weather events such as cloud cover and fog are big problems and compromise the usability of optical remote sensing and make the image processing more complicated [1]. To overcome those problems, the pattern of pixel values determined from substantial remote sensing data within a region can aid the reconstruction of data that is contaminated on account of the presence of clouds [2, 3].

Scientific research has been done on the detection and removal of clouds and their shadows from remote sensing images acquired by various sensors [4–8]. One of

common approaches for cloud removal is to generate composite image by selecting non-cloud pixels from satellite image time series [4, 6, 7, 9]. However, a drawback of multi-temporal image composition is residual in cloud-contaminated regions, since some types of landcover may rapidly change over time period [10]. Other method was based on regression trees to predict pixel values underneath clouds and cloud shadows in reference scenes from other scene dates [11]. However, in [11] the regression tree model only considers DN value of image, other parameters such as weather parameters, solar radiation which affect spectral radiance measured by satellite sensor are not taken into account.

In recent years, the US Geological Survey (USGS) provides a huge number of free satellite imagery online. As a result, many studies have shown the interest of utilizing multi-temporal satellite images [12–14]. [2] used multitemporal Landsat images to reconstruct imagery data covered by cloud based on local spectro-temporal relationships between considered image and reference images based on contextual prediction process. This contextual prediction process was implemented by linear predictors or by single non-linear prediction based on the support vector machines (SVM) [2]. [13] also took advantages of Landsat image time series to remove cloudy portions of an image and then reconstructed missing imagery data by cloning information from a set of reference images based on temporal correlation [13]. To obtain the temporal correlation, both of these methods used information in the neighborhood of the cloudy area, which may not always represent the information covered by cloud, especially in rapid change areas or heterogeneous regions [2, 13]. [3] used a large number of Landsat images to simulate an image acquired on a certain date by apply multi-linear regression between spectral radiance and eight parameters including air temperature, humidity, visibility, rainfall, Normalized Difference Vegetation Index (NDVI), direct solar radiation, diffuse solar radiation, reflected radiation. This prediction model does not depend on information around the predicted pixels [3]. However, this multi-linear regression may not fit the pattern well, a non-linear function could be considered to improve the prediction [3]. Unfortunately, estimating parameters of a non-linear model is not a trivial task. One solution for this problem is to replace the non-linear function by an Artificial Neural Network (ANN), which has been proved to be an efficient technique to approximate a non-linear function [15–17], but has been rarely used in reconstructing imagery data covered by cloud. Among the learning functions of neural networks, back-propagation algorithm has been used very popularly. However, Bayesian learning can provide more optimal and robust approximations [18].

Therefore, this study attempted to investigate potential application of Bayesian Neural Network (BNN) in retrieving pixel values underneath clouds by taking advantage of available dataset containing large amount of multi-date Landsat images to reconstruct missed data covered by cloud. To achieve this, BNN was used to model the relationship between eight variables including: air temperature, humidity, visibility, rainfall, NDVI, direct solar radiation, diffuse solar radiation, reflected radiation and spectral radiance of each pixel. The fitted model was used to predict values of the pixels covered by cloud. The cloud-free composite image was compared to actual image for quality assessment.

2 Study Site and Data

A $18 \text{ km} \times 18 \text{ km}$ area partly covering Iksan and Gimje in the Republic of Korea, which is approximately 180 km south of Seoul (see Fig. 1), was chosen to test the proposed method. Agricultural fields occupy most of the study area; however, it additionally includes a few high-rise residential areas and some public and commercial buildings, and is partly covered by forest areas. This area was selected because of the availability of quality Landsat images covering the area and the available meteorological data. There are two meteorological ground stations (indicated by red triangles in Fig. 1) close to the area, from which we can obtain details meteorological data. Furthermore, it is a developing region covered by various landcover types, which means that the landcover can changes significantly, so that the ability of the proposed method can be explored.

Korea has four very distinct seasons: spring, which is from March to the end of May; summer, which is from June through August; autumn, which is from September through November; and winter, which is from December to the end of February [19]. Spring begins with the sprouting of various species of trees and the first crops of strawberries. Summer is relatively hot and humid and may feature clouds and frequent rainfall for one to three weeks. In autumn, as the season progresses, the leaves change

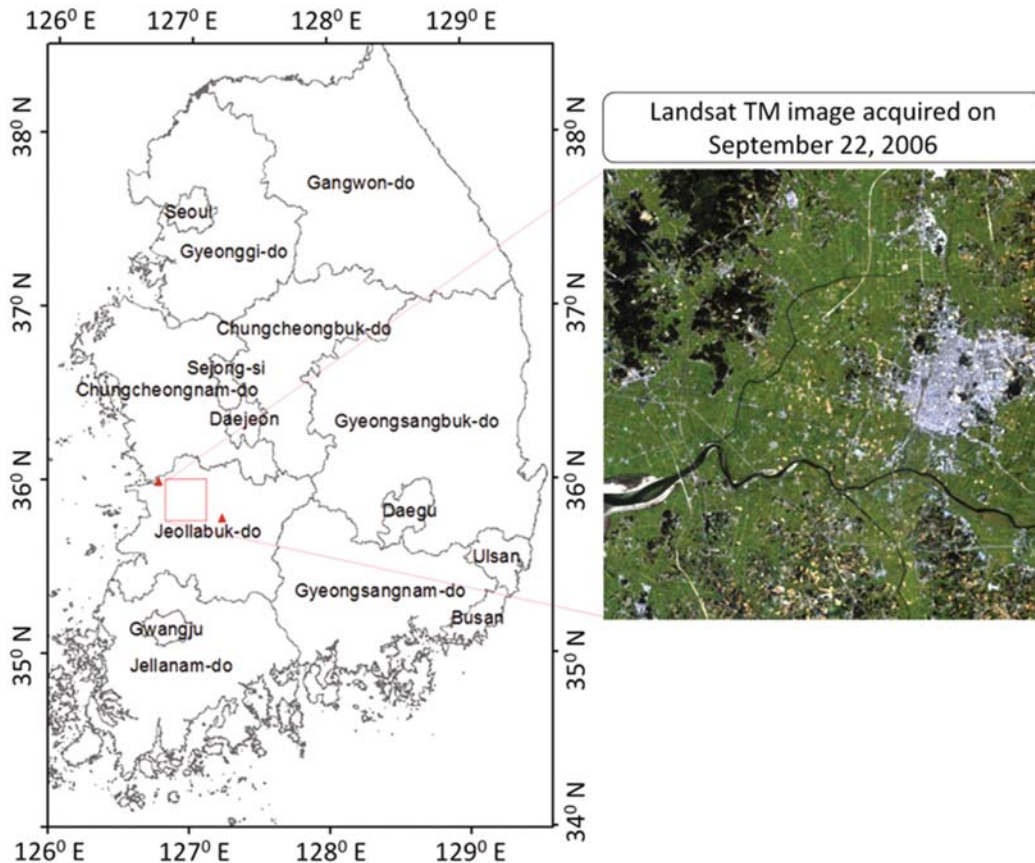


Fig. 1. Study area and Landsat image acquired on September 22, 2006.

colors and harvesting begins. Winter is generally cold and dry, and snow typically occurs in December and January. Therefore, to reconstruct missing data on a sub-Landsat image acquired on September 22, 2006, a dataset of 25 Landsat images acquired from May to November of 1994 to 2016 was used. Nineteen Landsat 5 Thematic Mapper (TM) images, three Landsat 7 Enhanced Thematic Mapper Plus (ETM+) images, three Landsat 8 images, and ASTER Global DEM (GDEM) were freely obtained from the USGS (<http://earthexplorer.usgs.gov/>). All of these images have spatial resolution of 30 m. Along with this dataset, meteorological data (i.e., air temperature, humidity, rainfall, and visibility) at two ground stations near the study area were collected from the Korean Meteorological Administration (KMA) (<http://www.kma.go.kr>). For each parameter, value measured by the two stations on acquisition time was averaged.

3 Methodology

3.1 Background of Bayesian Neural Network

A BNN is a kind of ANN with a prior distribution in its weights [20]. An ANN is a computational model based on the structure and functions of human brain. It is able to learn from information that flows through the network, then generalization and prediction can be performed [17]. After “learning” the ANN can provide the unknown relation f between the input vectors $X = [X_{i1}, X_{i2}, \dots, X_{ip}]$ and the output vector $Y = [Y_{i1}, Y_{i2}, \dots, Y_{iq}]$ as Eq. (1) [17]:

$$Y = f(X). \quad (1)$$

BNN was developed based on Bayes’ theorem [20]. Generally, the training step is aimed at reducing the sum squared error of the model output and target value [18]. Hyper-parameter values can be automatically estimated, and the uncertainty ones can be marginalized based on the posterior distribution [21]. The posterior probability for the parameter α can be written according to Bayes’ rules as Eq. (2) [22].

$$p(\alpha|D, M) = \frac{p(D|\alpha, M)p(\alpha|M)}{p(D|M)}. \quad (2)$$

where D is the data of the training set; M is the neural network model; $p(\alpha|D, M)$ is the likelihood of the parameters; and $p(\alpha|M)$ is the prior probability of α ; $p(D|M)$ is normalizing factor, which is also called evidence for the model M and can be expressed by Eq. (3) [22].

$$p(D|M) = \int_{\alpha} p(D|\alpha, M)p(\alpha|M)d\alpha. \quad (3)$$

Bayesian regularization generates a sequence of weights in the network parameter space in relation to the given data set and the network model. Then unnecessary linkage

weights are effectively reduced to zero. The network will calculate and train on the nontrivial weights, also known as the effective number of parameters, which will converge to a constant as the network grows [23]. Consequently, it can be optimized and can provide more optimal solution [18, 22].

3.2 Data Preprocessing

Several preprocessing steps were carried out before the data reconstruction takes place. USGS provides the Landsat imagery with digital number (DN). Therefore, radiometric calibration was conducted by using Eq. (4) to convert the DNs into spectral radiance [24].

$$L = Gain \times DN + Bias. \quad (4)$$

where L is the radiance of the pixel; DN is the digital number of the pixel; $Gain$ is the gain for a specific band; $Bias$ is the bias for a specific band; $Gain$ and $Bias$ can be obtained from the metadata file.

After the conversion, subset containing 600 pixel \times 600 pixel images was then clipped. To increase the number of satellite images, some Landsat images with a small amount of cloud cover were also included (maximum cloud coverage of selected images is 10%). Therefore, it was necessary to mask cloud pixels before the analysis. To do this, algorithm described by [25] was applied to generate cloud mask of used images. In addition, the dataset contained images acquired at different times; therefore, a shadow cast by high features, such as high buildings and mountains, was also different. To reduce this effect, a shadow mask for each image was additionally created based on ASTER GDEM with spatial resolution of 30 m using the method described in [26]. To reconstruct missing data, solar radiation including direct solar radiation, diffuse solar radiation, reflected radiation were used as predictor variables. The Solar radiation is estimated by Eq. (5) to (7) based on method described in [27].

$$I_{dir} = I_0 \tau_b \cos i. \quad (5)$$

$$I_{diff} = I_0 (0.271 - 0.294 \tau_b) \cos^2 \frac{\beta}{2} \sin \alpha. \quad (6)$$

$$I_r = r I_0 (0.271 + 0.706 \tau_b) \sin^2 \frac{\beta}{2} \sin \alpha. \quad (7)$$

where I_{dir} is direct solar radiation; I_{diff} is diffuse solar radiation; I_r reflected solar radiation; I_0 is extraterrestrial radiation; τ_b is atmospheric transmittance for beam radiation; r is ground reflectance coefficient; i is angle between the normal to the surface and the direction to the Sun; β is slope of the surface, and α is solar elevation angle.

3.3 Reconstruction of Contaminated Pixels by BNN

The spectral radiance measured by a sensor is affected by many components [28, 29]. Therefore, the correlation between the at-sensor radiance and the impact factors is very

complex. In brief, the complex relationship of measured radiance and impact factors can be expressed as a nonlinear or linear function. Due to the simplicity, the linear model is usually preferred. [3] used multi-linear regression to simulate Landsat image based on temporal correlation between the pixel values and eight important factors including air temperature (T), humidity (H), visibility (V), and rainfall (R), NDVI for every input image was computed by Eq. (8) [30], direct solar (DR), diffuse solar (DFR), and reflected radiation (RR). Here, the temperature, humidity, rainfall, and visibility are single values; NDVI, direct solar radiation, diffuse solar radiation, and reflected radiation are spatially distributed parameters. NDVI is used as a solution to reduce the effects of landcover changes. The equation obtained from the multilinear regression can be expressed as Eq. (9) [3].

$$NDVI = \frac{L_{NIR} - L_{Red}}{L_{NIR} + L_{Red}}. \quad (8)$$

where L_{NIR} and L_{Red} is spectral radiance of NIR and Red band of the Landsat images.

$$\begin{aligned} L_{(i,j,b)}^t = & a_{1(i,j,b)}T^t + a_{2(i,j,b)}H^t + a_{3(i,j,b)}V^t + a_{4(i,j,b)}R^t + a_{5(i,j,b)}NDVI_{(i,j)}^t \\ & + a_{6(i,j,b)}RR_{(i,j)}^t + a_{7(i,j,b)}DR_{(i,j)}^t + a_{8(i,j,b)}DFR_{(i,j)}^t + a_{9(i,j,b)}. \end{aligned} \quad (9)$$

where L is spectral radiance; t is acquisition time.

i, j , and b are the row, column, and band indices, respectively.

a_1 through a_9 are the regression coefficients.

However, as mentioned above, there are many factors affecting the radiance measured by a satellite sensor. The fact that it can be expressed by non-linear equations [28, 29]. Therefore, a linear model may not provide a suitable approximation. Whereas, a complex nonlinear function can provide a more accurate prediction [3]. Consequently, more complex mixing models need to be considered. However, estimating non-linear model requires complex analysis with multiple-step algorithms. One of optimal solutions is to replace the non-linear function by an ANN, which can handle the nonlinear correlation well [15–17]. There are various types of neural networks, such as feed-forward neural network, BNN, stochastic neural network, recurrent neural network [17]. However, BNN can provide more optimal and robust approximations [18, 23].

In this study, BNN was used to model complex relationships between spectral radiance measured by satellite sensor and eight variables including air temperature (T), humidity (H), visibility (V), and rainfall (R), NDVI, direct solar (DR), diffuse solar (DFR), and reflected radiation (RR). Generally, it can be expressed by Eq. (10). NDVI for every input image was computed from Red and NIR band of the Landsat images by Eq. (8) [30], NDVI on target date requiring the reconstruction of missing imagery data can be interpolated from images obtained during the same season.

$$L_{(i,j,b)}^t = f \left[T^t, H^t, V^t, R^t, NDVI_{(i,j)}^t, DR_{(i,j)}^t, DFR_{(i,j)}^t, RR_{(i,j)}^t \right]. \quad (10)$$

where L is spectral radiance; t is acquisition time.

i, j , and b are the row, column, and band indices, respectively.

a_1 through a_9 are the regression coefficients.

Before training the networks, the selection of the number of hidden layer and hidden neurons is very important [31]. This depends on the complexity of the relation f to be modeled and the fact that there is no standard for choosing them [32]. In this study, after many trials, the network was designed to use 1 hidden layer with 4 hidden neurons as illustrated in Fig. 2. To train the network, various training algorithms are available [33, 34]. In this study, after many trials the network was trained using Bayesian Regularization function with 500 epochs, which showed the best performance in this case study.

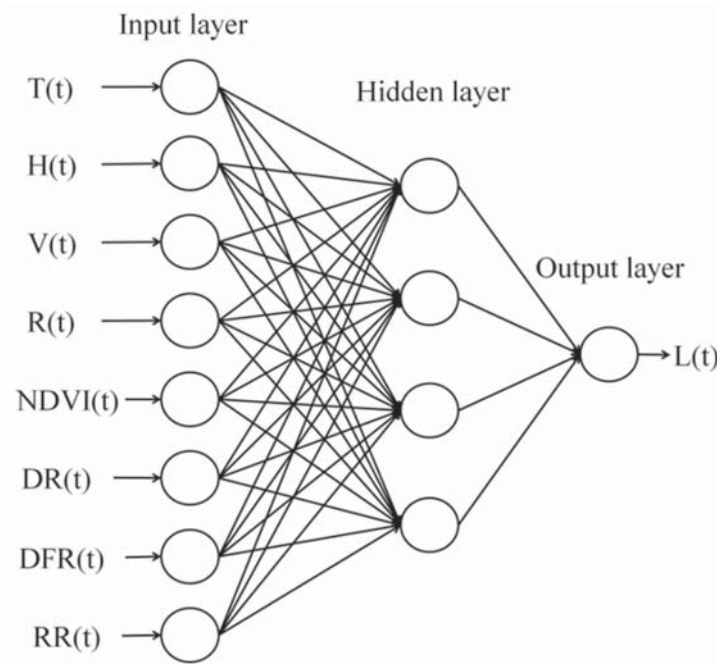


Fig. 2. Architecture of BNN used in this study.

3.4 Quality Assessment

In order to verify the retrieved imagery data, both visual comparison and quantitative analysis were used. Visually, the cloud-free image generated by the proposed method was compared to the actual image. For quantitative analysis, Spectral Correlation Mapper (SCM) [35] was used to assess the difference between a retrieved pixel compared with the corresponding actual pixel. The SCM method employs Pearson's correlation coefficient (R) computed by Eq. (11) to detect changes [35]. R values range from -1 to $+1$. Large values indicate that two spectra are similar. The value of 1 indicates that there is no difference between the two spectra.

$$R = \frac{\sum_{i=1}^{nb} (T1_i - \overline{T1})(T2_i - \overline{T2})}{\sqrt{\sum_{i=1}^{nb} (T1_i - \overline{T1})^2 \sum_{i=1}^{nb} (T2_i - \overline{T2})^2}}. \quad (11)$$

where $T1$ and $T2$ $\overline{T1}$ and $\overline{T2}$ are the spectra of a certain pixel in each band in the first and the second images, respectively; $\overline{T1}$ and $\overline{T2}$ are the mean values of $T1$ and $T2$ of each pixel; nb is the number of bands in an image.

4 Methodological Flowchart

A cloud-free sub-Landsat image acquired on September 22, 2006 (see Fig. 4(a)) was selected as a target image which was required missing imagery data reconstruction. This date was selected because it is in the middle of the acquisition period of the dataset; additionally, the image on this date was clear, so that it is good for quality assessment. Three portions of this image were masked in assumption that they were covered by cloud (see Fig. 4(b), where white zones denote cloud regions, which means pixels' value within those areas need to be reconstructed): area #1 was almost covered by forest; area #2 was an urban region; area #3 was a mixed area almost covered by agricultural fields and small amount of man-made structures. To test the proposed model, the experiment was carried out by five main steps as shown in Fig. 3: 1. Preprocessing; 2. BNN training; 3. Reconstructing missing imagery data; 4. Histogram

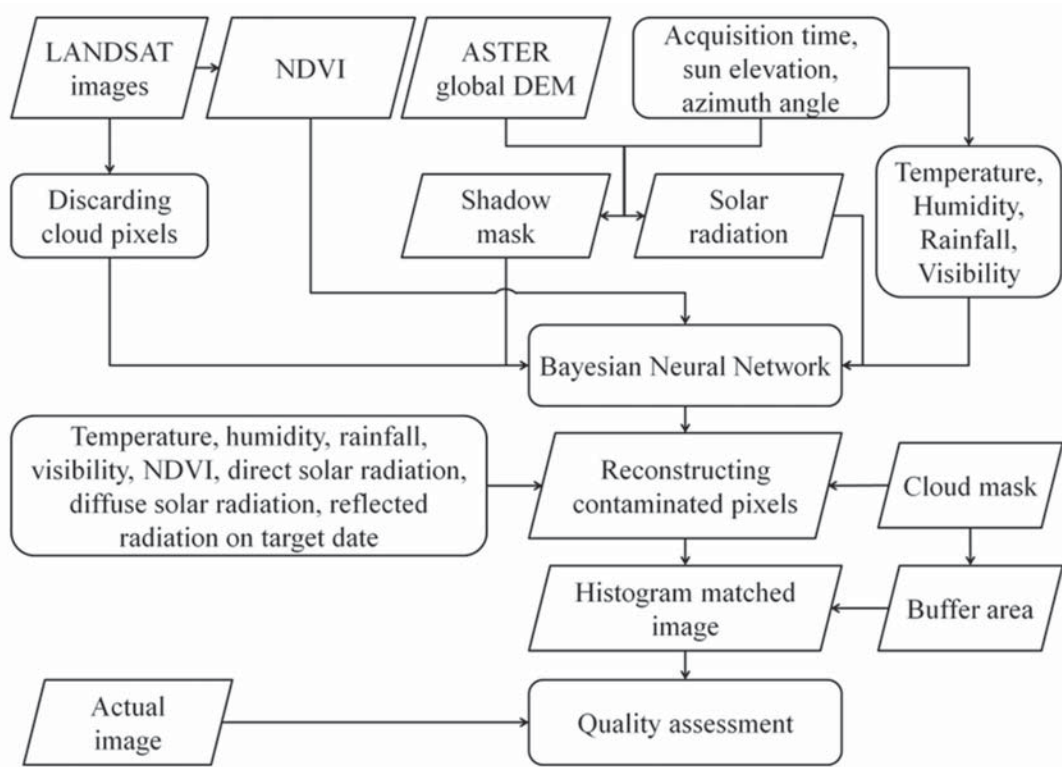


Fig. 3. Methodological flowchart.

matching; 5. Quality assessment. After aforementioned preprocessing steps, cloud masks, shadow masks as well as solar radiations were obtained. After that, BNN illustrated by Fig. 2 was trained for every contaminated pixel. In this step the shadow pixels and cloudy pixels in the input images were excluded based on the masks generated in the preprocessing phase. Subsequently, the obtained model expressing the relationship between measured radiance and the eight predictor variables (i.e. air temperature, humidity, rainfall, visibility, NDVI, direct solar radiation, diffuse solar radiation and reflected radiation) was used to reconstruct pixels' value covered by cloud on September 22, 2006. Finally, the reconstructed image was compared to the actual image for quality assessment. In order to reduce color difference between reconstructed pixels and the surrounding actual pixels, histogram matching was conducted base on a 10-pixel buffer around the masking areas.

5 Results and Discussions

The experiment was implemented by using MATLAB programming language. After many attempts, the network with 1 hidden layer and 4 hidden neurons was trained using Bayesian Regularization function, number of epochs was set to 500, the transfer function for the hidden layer and the output layer was tan-sigmoid and linear function, respectively. The processing was implemented by using MATLAB Neural Network Toolbox. The trained network was used to generate new pixels' value within the three cloud regions of the cloud mask described in Fig. 4(b). Then the old pixels were replaced with the new pixels to generate a cloud free image on September 22, 2006 as shown in Fig. 4(d). In this study, NDVI on September 22, 2006 was linearly interpolated from the NDVIs on August 31, 2004 and October 24, 2006. In order to reduce the color difference between the reconstructed area and the surrounding area, histogram matching was performed solely on each cloud cover region based on adjacent pixels of 10-pixel buffer around each masking area. The result after histogram matching was illustrated in Fig. 4(e).

Visual comparison between the actual image (Fig. 4(a)) and the reconstructed image (Fig. 4(d)) showed that the reconstructed pixels and the actual pixels are very similar in man-made area (Area #2). However, the color similarity is declined slightly in forest area (Area #1), and the most color difference appears in mixed area (Area #3). This could be due to the vegetation changed much over time. However this difference was almost overcome after conducting histogram matching based on the buffer areas (see Fig. 4(e)). For quantitative assessment, the SCM was carried out on non-corrected images. The results of SCM were shown in Fig. 5 and Table 1.

Figure 5 and Table 1 proved that the pixels generated by the proposed algorithm are very similar to the actual pixels, especially in urban area, where can be considered as non-change area. The similarity is illustrated by the high average of R in all three areas, and the large amount of pixel has R over 0.99, which can be considered as no difference between the two pixels. Actually, the highest percentage of R over 0.99 is approximate to 91% in urban area. In the other two areas, the percentages of R over 0.99 are also quite high, about 78%. If considering the pixel with R over 0.98 is almost similar, the percentages of these pixels were much greater: the lowest value is 92.8%

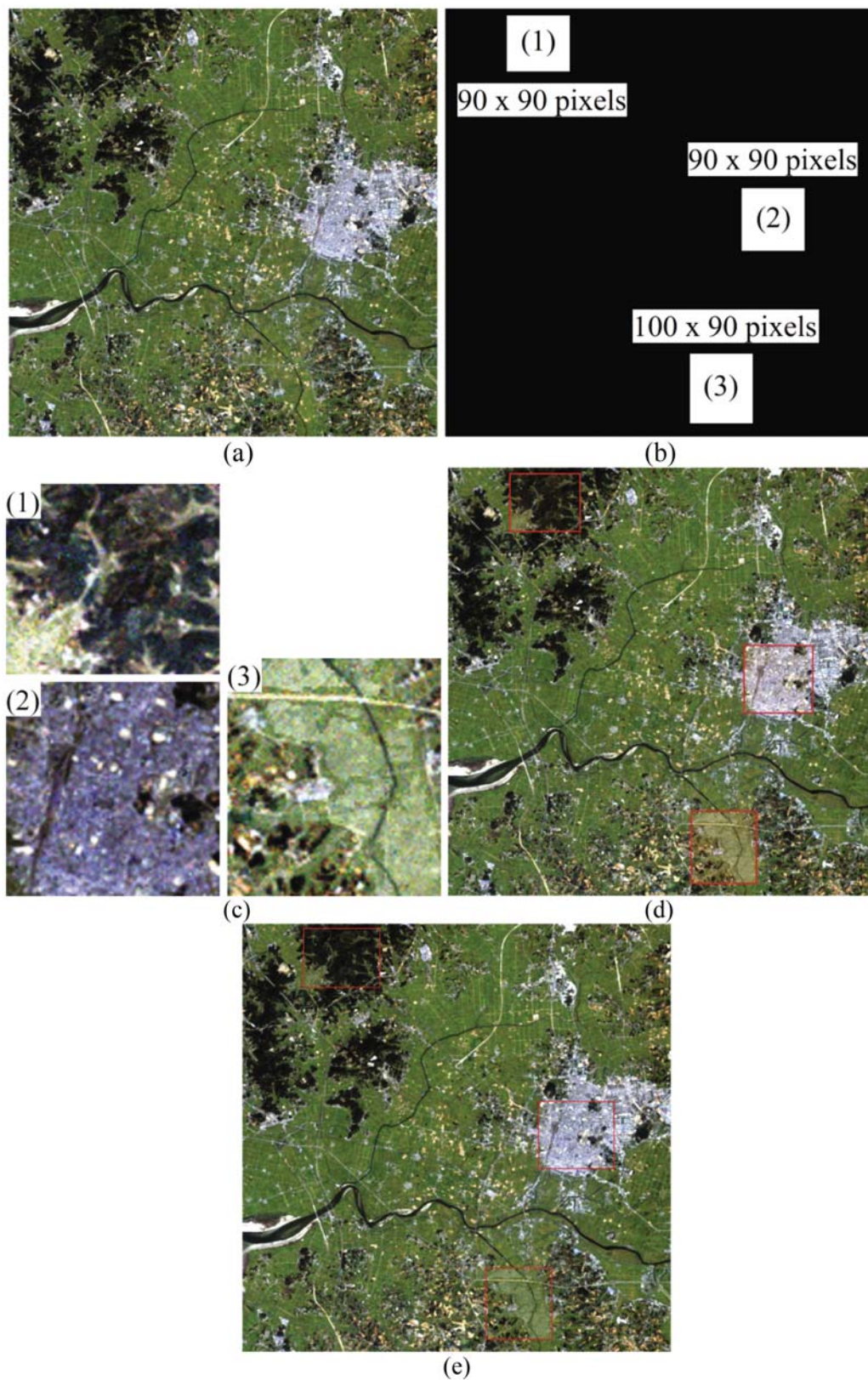


Fig. 4. (a) Original image; (b) cloud mask; (c) three reconstructed areas; (d) reconstructed image; (e) histogram matched image; Red rectangles denote the reconstructed areas.

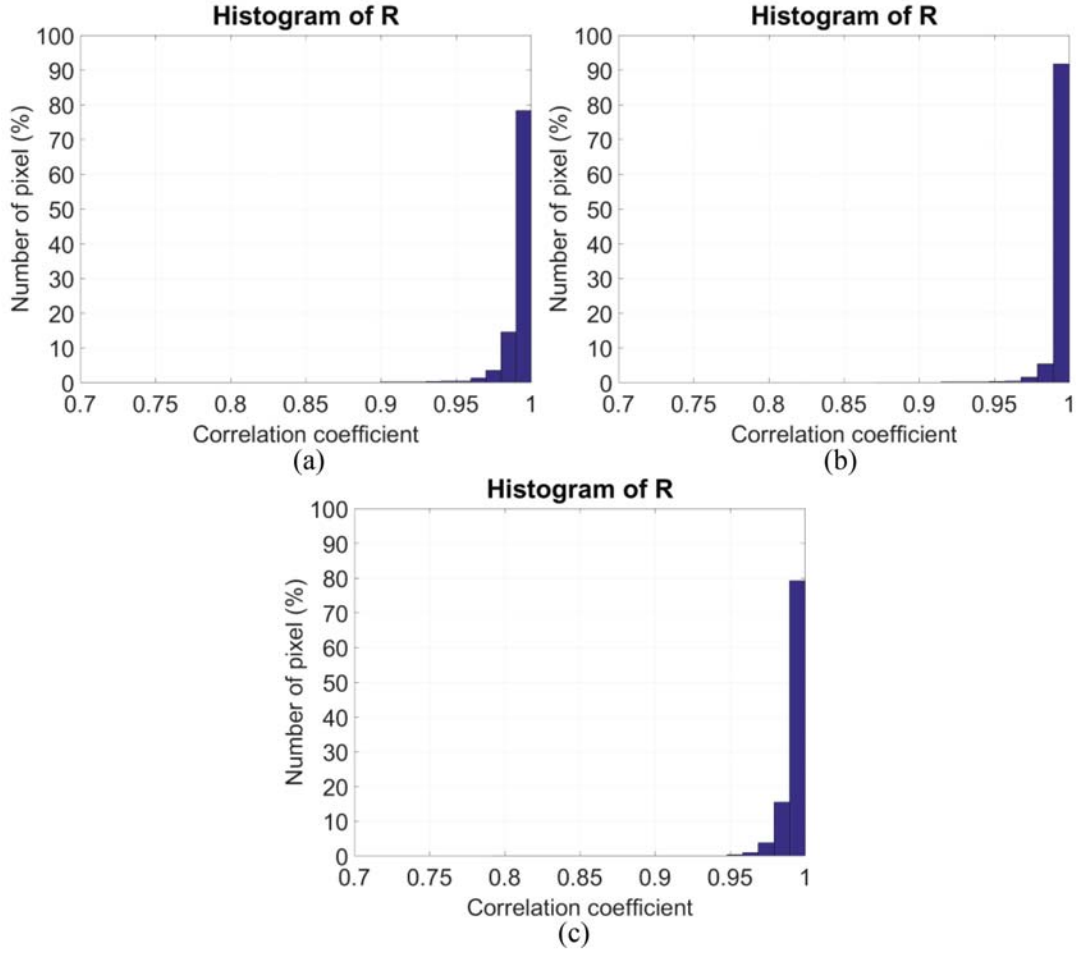


Fig. 5. Correlation coefficients between reconstructed image and actual image on September 22, 2006: (a) area #1; (b) area #2; (c) area #3.

Table 1. Summary of Correlation coefficients.

	Area 1	Area 2	Area 3
Mean	0.993	0.995	0.992
Max	1.000	1.000	1.000
Min	0.792	0.871	0.629
Percentage of pixel (%)			
$R > 0.99$	78.0	90.9	78.1
$R > 0.98$	94.1	96.6	92.8
$R < 0.95$	0.4	0.7	1.9

for mixed area, and the greatest value is 96.1% for man-made area. Meanwhile, percentage of pixels with $R < 0.95$ are close to zero in area #1 and #2, and it is just 1.9% in area #3.

Visually and quantitatively, the results generated by the proposed method are very similar to those in the actual image. This seems to be better than image composite

based methods such as [6, 7, 9]. Additionally, owing to its flexibility, the proposed method can be used to reconstruct pixels' value contaminated by cloud on any date within the period of acquisition time of input images. However, similar to other multitemporal-based method such as [13, 36], missing imagery data reconstructed by the proposed method was mainly affected by landcover changes. As a result, the percentage of pixels, whose R greater than 0.99, which can represent a state of no difference, is highest in urban area, where change slowly over time. This was reduced dramatically in the other two areas, where were mostly covered by vegetation, which changes seasonally. Noticeably, unlike method of [13, 36], the pixels' value predicted by the proposed method did not depend on information around them, the buffer areas were only used to improve visualization. Furthermore, by taking advantage of BNN, the proposed approach can obtain appropriate temporal correlation to reconstruct missing information, and thus, it can potentially yield better results in terms of radiometric accuracy. However, more quantitative analysis and comparison are needed to make widespread use of the proposed method.

Unlike simple linear model, the non-linear model requires multiple-step solutions. As a result, it takes more time to train the BNN. However, reconstructing pixels' value covered by cloud is usually carried out on small portions of images. Therefore, the time requirement for training the model is not a big problem. Additionally, the modern computer systems are more and more powerful that can minimize the difficulty in training the BNN.

6 Conclusion

This paper proposed an approach to reconstruct pixels' value contaminated by cloud in a remote sensing image by taking advantage of a dataset containing a large amount of image time series and BNN. The proposed method was used to generate new pixels' value where covered by cloud of a Landsat image acquired on September 22, 2006. The result showed that reconstructed pixels' value were similar to the actual value in non-change area with the percentage of R over 0.99 is about 91%. However, the similarity reduced in areas which changed significantly over time period. The color difference between reconstructed areas and the rest of image was almost overcome after running histogram matching based on the buffer of 10-pixel surrounding the cloud masks.

The similarity of the retrieved imagery data and the actual ones indicates that the BNN can be an effective technique for recovering the original pixels' value where were covered by cloud. However, more quantitative comparisons with other related techniques are necessary to bring BNN into more widespread use in this field. Additionally, like other multitemporal-based methods, limitation of the proposed method is its sensitivity to changes in land cover during the period in which the input satellite images were acquired. Nevertheless, given its flexibility, the proposed method can be reconstruct pixels' value covered by cloud on any date within the period of acquisition time of input images. Although, the results of SCM can prove the reliability of the proposed method, further study is still needed to reduce the effect of landcover changes on predicting new pixels' value.


Acknowledgement. This work was supported by Vietnam National Foundation of Science and Technology Development under the project 105.99-2014.15.

References

1. Ju, J., Roy, D.P.: The availability of cloud-free Landsat ETM + data over the conterminous United States and globally. *Remote Sens. Environ.* **112**, 1196–1211 (2008)
2. Melgani, F.: Contextual reconstruction of cloud-contaminated multitemporal multispectral images. *IEEE Trans. Geosci. Remote Sens.* **44**, 442–455 (2006)
3. La, H.P., Eo, Y.D., Lee, S., Park, W.Y., Koo, J.H.: Image simulation from multitemporal landsat images. *GISci. Remote Sens.* **52**, 586–608 (2015)
4. Liew, S.C., Li, M., Kwoh, L.K., Chen, P., Lim, H.: Cloud-free multi-scene mosaics of SPOT images. In: *International Geoscience and Remote Sensing Symposium 2*, pp. 1083–1085. IEEE Press, Seattle (1998)
5. Abd-Elrahman, A., Shaker, I.F., Abdel-Gawad, A.K., Abdel-Wahab, A.: Enhancement of cloud-associated shadow areas in satellite images using wavelet image fusion. *World Appl. Sci.* **4**, 363–370 (2008)
6. Tseng, D.C., Tseng, H.T., Chien, C.L.: Automatic cloud removal from multi-temporal SPOT images. *Appl. Math. Comput.* **205**, 584–600 (2008)
7. Gui, Z., Chen, F., Yang, J., Li, X., Li, F., Zhao, J.: Automatic cloud and cloud shadow removal method for landsat TM images. In: *10th International Conference on Electronic Measurement & Instruments (ICEMI)*, pp. 80–84. IEEE Press, Chengdu (2011)
8. Jin, S., Homer, C., Yang, L., Xian, G., Fry, J., Danielson, P., Townsend, P.A.: Automated cloud and shadow detection and filling using two-date Landsat imagery in the USA. *Int. J. Remote Sens.* **34**, 1540–1560 (2013)
9. Li, M., Liew, S., Kwoh, L.: Automated production of cloudfree and cloud shadow-free image mosaics from cloudy satellite imagery. In: *20th Congress of the International Society of Photogrammetry and Remote Sensing*, pp. 15–23 (2004)
10. Gui, Z., Liu, J., Chen, F.: Automatic local phenology simulation for landsat TM image. In: *2012 IEEE International Conference on Information Science and Technology*, Wuhan, Hubei, China (2012)
11. Helmer, E.H., Ruefenacht, B.: Cloud-free satellite image mosaics with regression trees and histogram matching. *Photogram. Eng. Remote Sens.* **9**, 1079–1089 (2005)
12. Hwang, T., Song, C., Bolstad, P.V., Band, L.E.: Downscaling real-time vegetation dynamics by fusing multi-temporal MODIS and Landsat NDVI in topographically complex terrain. *Remote Sens. Environ.* **115**, 2499–2512 (2011)
13. Lin, C.-H., Tsai, P.-H., Lai, K.-H., Chen, J.-Y.: Cloud removal from multitemporal satellite images using information cloning. *IEEE Trans. Geosci. Remote Sens.* **51**, 232–241 (2013)
14. Guyet, T., Nicolas, H.: Long term analysis of time series of satellite images. *Pattern Recogn. Lett.* **70**, 17–23 (2016)
15. Harter, F.P., de Campos Velho, H.F.: New approach to applying neural network in nonlinear dynamic model. *Appl. Math. Model.* **32**, 2621–2633 (2008)
16. Xiong, C., Li, T.: Application of artificial neural networks to prediction of deformation in deep foundation pit. In: *2011 International Conference on Multimedia Technology (ICMT)*, pp. 1448–1453. IEEE Press, Hangzhou (2011)
17. Amato, F., Havel, J., Gad, A.-A., El-Zeiny, A.M.: Remotely sensed soil data analysis using artificial neural networks: a case study of el-fayoum depression, Egypt. *ISPRS Int. J. Geo-Inf.* **4**, 677–696 (2015)

18. Ticknor, J.L.: A Bayesian regularized artificial neural network for stock market forecasting. *Expert Syst. Appl.* **40**, 5501–5506 (2013)
19. KMA. http://web.kma.go.kr/eng/biz/climate_01.jsp
20. MacKay, D.J.C.: Bayesian interpolation. *Neural Comput.* **4**, 415–447 (1992)
21. Hernández-Lobato, J.M., Adams, R.P.: Probabilistic backpropagation for scalable learning of Bayesian neural networks. In: 32nd International Conference on Machine Learning, vol. 37, pp. 1861–1869. JMLR, Lille (2015)
22. Lampinen, J., Vehtari, A.: Bayesian approach for neural networks – review and case studies. *Neural Netw.* **14**, 7–24 (2001)
23. Burden, F., Winkler, D.: Bayesian regularization of neural networks. *Methods Mol. Biol.* **458**, 25–44 (2008)
24. Chander, G., Markham, B.: Revised Landsat-5 TM radiometric calibration procedures and postcalibration dynamic ranges. *IEEE Trans. Geosci. Remote Sens.* **41**, 2674–2677 (2003)
25. Ouaidrari, H., Vermote, E.F.: Operational atmospheric correction of landsat TM data. *Remote Sens. Environ.* **70**, 4–15 (1999)
26. Ratti, C., Richens, P.: Raster analysis of urban form. *Environ. Plan.* **31**, 297–309 (2004)
27. Kumar, L., Skidmore, A.K., Knowles, E.: Modelling topographic variation in solar radiation in a GIS environment. *Int. J. Geogr. Inf. Sci.* **11**, 475–497 (1997)
28. Photon Research Associates: GCI Toolkit Manual. Photon Research Associates, San Diego, CA (1998)
29. Schott, J.R.: *Remote Sensing: The Image Chain Approach*, 2nd edn. Oxford University Press, New York (2007)
30. Rouse, J.W., Haas, R.H., Schell, J.A., Deering, D.W.: Monitoring vegetation systems in the great plains with ERTS. In: 3rd ERTS Symposium, pp. 309–317. NASA SP-351, NASA, Washington, DC (1974)
31. Pham, B.T., Bui, D.T., Prakash, I., Dholakia, M.B.: Hybrid integration of Multilayer Perceptron Neural Networks and machine learning ensembles for landslide susceptibility assessment at Himalayan area (India) using GIS. *CATENA* **149**, 52–63 (2017)
32. Maduako, I.D., Yun, Z., Patrick, B.: Simulation and prediction of land surface temperature (LST) dynamics within Ikom City in Nigeria using artificial neural network (ANN). *J. Remote Sens. GIS* **5**, 1–7 (2016)
33. Zupan, J.G.J.: *Neural Networks in Chemistry and Drug Design*, 2nd edn. Wiley VCH, Weinheim (1999)
34. Ahmed, F.E.: Artificial neural networks for diagnosis and survival prediction in colon cancer. *Mol. Cancer* **4** (2005)
35. Carvalho Júnior, O.A., Guimarães, R.F., Gillespie, A.R., Silva, N.C., Gomes, R.A.T.: A new approach to change vector analysis using distance and similarity measures. *Remote Sens.* **3**, 2473–2493 (2011)
36. Benabdelkader, S., Melgani, F., Boulemden, M.: Cloud-contaminated image reconstruction with contextual spatio-spectral information. In: *IEEE International Geoscience and Remote Sensing Symposium*, pp. 373–376, IEEE Press, Barcelona (2007)

Detection and Prediction of Urban Expansion of Hanoi Area (Vietnam) Using SPOT-5 Satellite Imagery and Markov Chain Model

Trung Van Nguyen¹ , Nam Van Nguyen^{2,3}, Ha Thu Thi Le¹,
Hien Phu La¹, and Dieu Tien Bui⁴

¹ Faculty of Geomatics and Land Administration,
Hanoi University of Mining and Geology, 18 Vien Street, Duc Thang Ward,
Bac Tu Liem District, Hanoi City, Vietnam
nguyenvantrung@hmg.edu.vn

² Faculty of Surveying and Mapping,
Hanoi University of Natural Resources and Environment, 41A Phu Dien Street,
Cau Dien Ward, Tu Liem District, Hanoi City, Vietnam

³ Moscow State University of Geodesy and Cartography, MIIGAiK #4,
Gorokhovskiy Pereulok, 105064 Moscow, Russia

⁴ GIS Group, Department of Business and IT,
University College of Southeast Norway,
Gullbringvegen 36, 3800 Bø i Telemark, Norway

Abstract. The main objective of this study is to detect and predict the urban area expansion at Hanoi, a typical urbanization city in Vietnam. For this purpose, firstly, temporal SPOT-5 images for years 2003, 2007, and 2011 were used to classify four land cover classes, open water, vegetation, barren, and residential area. Secondly, Impervious Surface Index (ISI) computed from the spectral bands of the above imagery. This index was then used to extract impervious surface information of the study area from residential area. Using the three derived land use/land cover maps, the area of land use/land cover types in the Hanoi area for years 2019 and 2027 were simulated and predicted using a Markov chain model. The results showed that the impervious surfaces of the Hanoi will increase 8.27% and 14.09% of total study area in 2019 and 2027, respectively. The results from this study provide valuable information to the local city planners in their urban planning and development.

Keywords: Hanoi city · Impervious surfaces · SPOT · Markov chain model · Urban

1 Introduction

Vietnam is considered as one of the countries that has the highest rate of urbanization in Southeast Asia due to the rapid development of economy [1]. The rate of urbanization is especially high for Hanoi and Ho Chi Minh cities where the population accounts for 16.8% (15 million people) of total population of the country [2]. For the case of Hanoi, the population increased from 3.2 million in 2003 to 6.3 million in 2007

[3] and to 7.216 million in 2015 with the urbanization rate is 49.1% [2]. The high rate of urbanization has resulted in complex problems such as reduced open space, environmental pollution, traffic overflows, and high pressure on the infrastructures [4]. Therefore, prediction of urban expansion for different future scenarios is highly necessary that helps the local planners useful information for their urban planning and development.

The aim of this study is to detect and predict the urban expansion in Hanoi area. For this purpose, SPOT-5 data for years 2003, 2007, and 2011 were used to derive four land cover classes, open water, vegetation, barren, and residential area. Since the sprawl of impervious surfaces may provide valuable information for planning urban in the future, therefore conversion from other LULC types to impervious surfaces was estimated. Accordingly, Impervious Surface Index (ISI) was also computed from the spectral bands of the above imagery, and then, the multi-temporal LULC maps, which include impervious surfaces, vegetation, open water, barren, and garden, were used for predicting LULC area types in future time.

In order to predict urban expansion, various method and techniques have been proposed such as knowledge experts, landscape metrics, agent based modelling, cellular automata, and machine learning [5]. However, Markov chain, a stochastic process system for predicting one status being changed to another known status [6], has proven a powerful and effective for prediction of urban changes [7], and therefore, this model was selected for this study. The main advantage of this method is that it has ability to summarize and analyze the change in urban land-use where changes of transition are estimated intern of probabilities. These probabilities are employed to predict and discover possible situations of future urban land use changes and urban expansion patterns.

2 Study Area and Data

Hanoi city is the capital of Vietnam that lines between latitudes $20^{\circ}30'30''\text{N}$ and $21^{\circ}20'30''\text{N}$, and longitudes $105^{\circ}20'30''\text{E}$ and $106^{\circ}05'30''\text{E}$ (Fig. 1). The city covers an area of about 3324.5 km^2 with the population of 7.216 million people in 2015 [2, 3]. The strong economic development has spurred expansions of industrial parks, urban construction and traffic system, and infrastructure for living people [8]. These are main causes of impervious surface expansion in this study area.

In this research, SPOT-5 images of Hanoi area in 2003, 2007 and 2011 (Table 1) were used. Acquisition dates of three SPOT-5 data were chosen with time step of 4 years for satisfying date requirement of Markov chain model. In addition, a land use map for the study area produced in 2010 at scale of 1:10,000 was provided by Center of Surveying and Map Data (COSAMD) was used. This map was used for evaluating the LULC maps derived from the aforementioned SPOT-5 images.

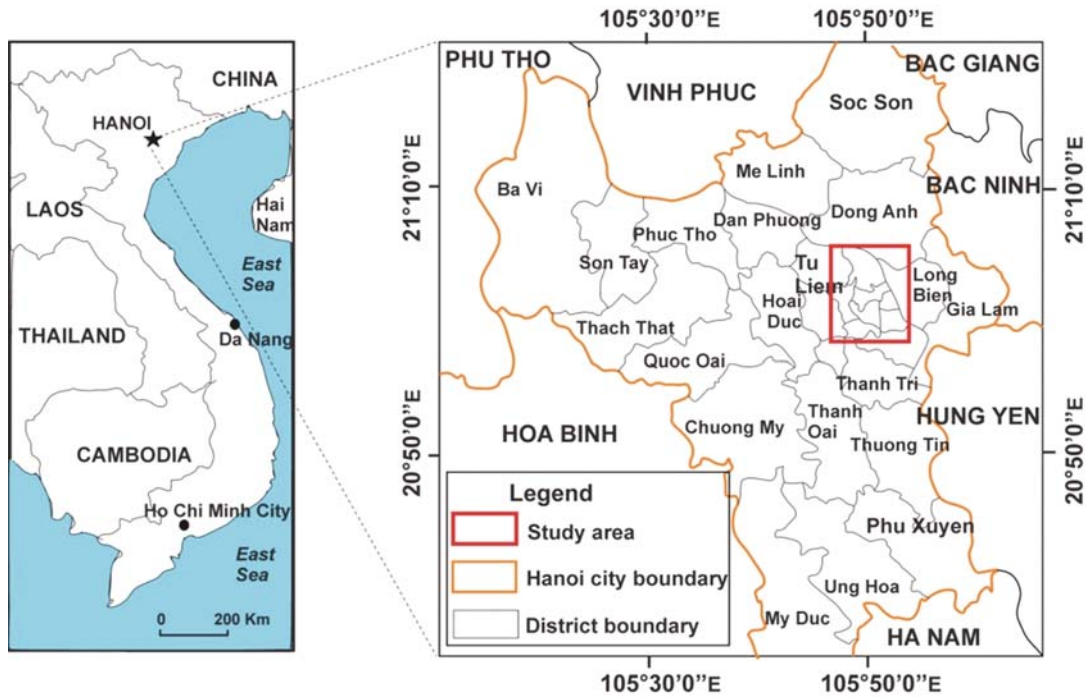


Fig. 1. Location of the study area, Hanoi city

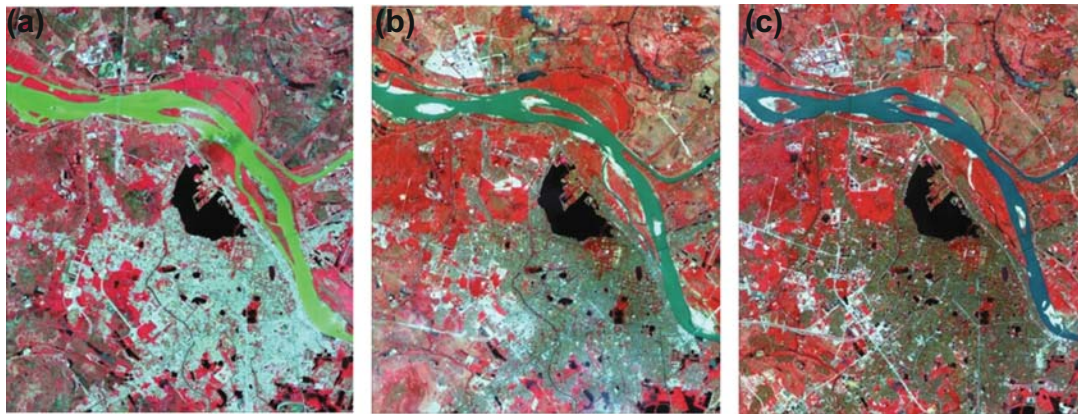


Fig. 2. SPOT-5 subset images of the study area: (a) 24/06/2003 (b) 21/08/2007 (c) 12/12/2011

Table 1. SPOT-5 satellite imagery used in this study

No.	Satellite	Sensor	Parth/Row	Date (dd/mm/yyyy)	Resolution (m)
1	SPOT-5	HRG	269/307	24/06/2003	10
2	SPOT-5	HRG	270/308	21/08/2007	10
3	SPOT-5	HRG	270/308	12/12/2011	10

3 Methodology

Methodological flowchart for this research consists of three main steps: (i) Object-oriented classification; (ii) Extraction of impervious surface; and (iii) Prediction of land use change based on Markov model (Fig. 3).

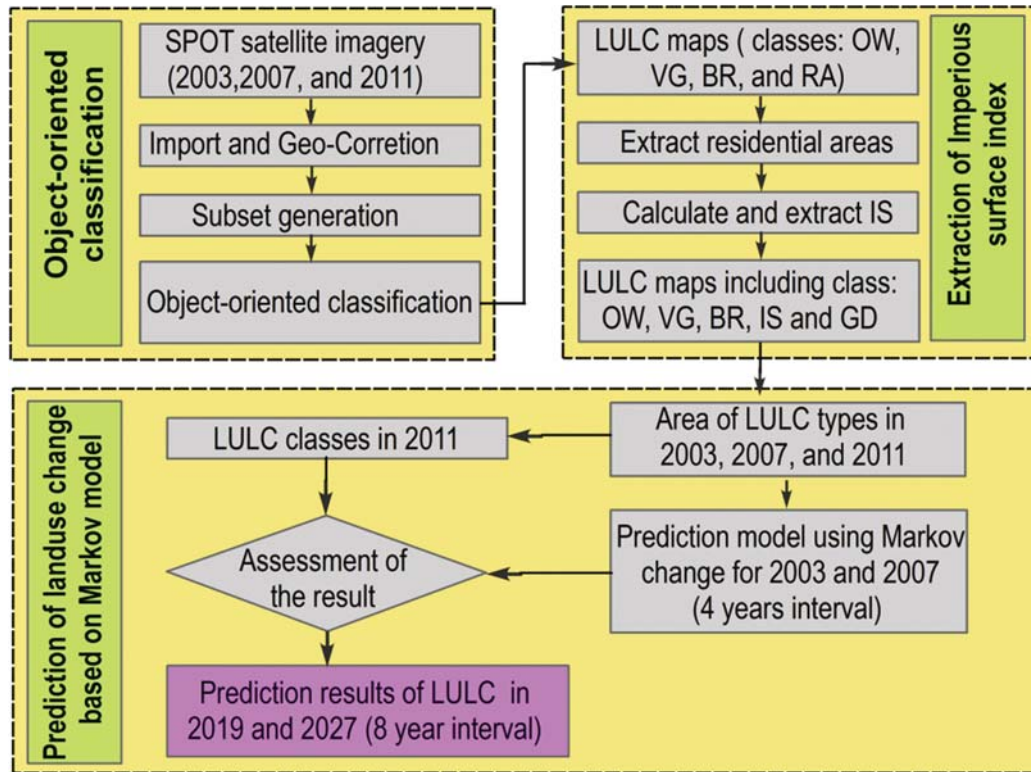


Fig. 3. Methodological flowchart for this research, OW: open water; VG: vegetation; BR: Barren; and RA: residential area.

3.1 Object-Oriented Classification

This step aims to derive four land cover classes, open water, vegetation, barren, and residential area for the three years 2003, 2007, and 2011 from the SPOT-5 data. Before the classification is conducted, a preprocessing process for these images was carried out. Because SPOT-5 images were acquired at level 1A, the SPOT-5 orbital Push-broom Model was used for geo-correcting SPOT-5 data with Ground Control Points (GCPs) derived from land use map at scale of 1:10,000. It should be noted that a digital elevation model for Hanoi was not used because this area is a quite flat. Then, these obtained images were projected to the UTM projection (VN2000) (Fig. 2). To solve the effects due to the different times of acquisition, the haze reduction and atmospheric correction for these images were also carried out. In the next step, the combination of homomorphic filter and the matching mean reflectance in both hazy/clear regions method was used for removing the haze of the SPOT-5 bands. As result, the surface reflectance images were retrieved by removing atmospheric effect by means of the retrieved aerosol

optical depth using MOTRAN 4.0 [9]. Finally, the contrast stretching and spatial filtering were used to enhance the quality of these images.

Once the preprocessing process has been completed, the object-oriented classification was carried out that includes multi-scale segmentation and classification steps. In the first step, the multi-scale segmentation was conducted for these SPOT-5 images using eCognition Developer 8.7 software [10]. The segmentation of the images into objects is based on three parameters: scale, shape, and compactness [11]. The scale directly affects the size of the segmentation objects, whereas, the shape value refers to the form and the structure of the individual objects and characterizes the spectral or spatial homogeneity of the resulting segmentation. Meanwhile, the compactness value is the ratio of an object's perimeter to the square root of the number of pixels within that image objects. This segmentation method is the most appropriate for the purpose of our work. For this research, the segmentations were conducted at a scale of 20, shape value of 0.3, and smoothness value of 0.5 and these values were found the best for the images data at hand.

Once the multi-scale segmentation has been completed, the classification of these image objects was carried out using hierarchical structures that describes the object's neighbor, its parent object, and its child objects. Features inherited from the parent object can transfer to the child objects. The user interacts with the procedure and based on statistics, texture, form and mutual relations among objects defines training areas. The classification of an object can then follow nearest neighbor method [12], and accordingly, each class of a classification scheme contains a class description. Each class description consists of a set of rule expressions allowing the evaluation of specific features and their logical operation. A rule can have one single condition or can consist of a combination of several conditions that have to be fulfilled for an object to be assigned to a class [13].

For this research, a total of four land cover classes including open water, vegetation, barren and residential area were identified based on the structural formation of the urban. Class rules for the objects were then developed using spectral signatures, shape, location and the contextual relationships of the objects. Samples for each class were selected from the image objects to act as training areas for the classification. Objects were assigned class rules using spectral signatures, shape and contextual relationships. The rules were then used as a basis for the classification of the data with the most probable/likely class being assigned to each object.

3.2 Extraction of Impervious Surface

In this section, four indicators including Soil Index (SI), Soil Adjusted Vegetation Index (SAVI), Normalized Difference Water Index (NDWI), Impervious Surface Index (ISI) were calculated as following [14]. To classify the four land cover classes, open water, vegetation, barren and residential area, the three indicators, SI, SAVI, and NDWI that computed from the spectral bands of the SPOT-5 imagery (Eqs. 1, 2, and 3) were then used to assign classes based on the rules. The Impervious Surface Index (ISI) derived from the spectral bands of the SPOT-5 imagery and NDVI (Eq. 5) was then used to extract impervious surface information of the study area from residential

area. Remaining part of residential area after extracting impervious surface was the garden area.

$$SI = (GREEN - BLUE) / (GREEN + BLUE) \quad (1)$$

where GREEN is spectral value of green band and BLUE is spectral value of blue band.

The soil adjusted vegetation index (SAVI) was used in this research because it could remove contamination associated with bare soil [15].

$$SAVI = [(NIR - RED)(1 + l)] / (NIR + RED + l) \quad (2)$$

where l = soil adjusted factor ranging from 0 and 1, however, in this research, we chose 0.5 to eliminate the impact of different background; RED is spectral value of red band; NIR is spectral value of near-infrared band.

Normalized difference water index (NDWI) was used because the SPOT data include both GREEN and NIR band. NDWI is calculated using equation as follows [16].

$$NDWI = (GREEN - NIR) / (GREEN + NIR) \quad (3)$$

where GREEN is spectral value of green band; NIR is spectral value of near-infrared band.

Impervious Surface Index (ISI) was introduced by [14] using four bands for each SPOT image (B1, B2, B3, and B4), and the offset I_j (I_1 , I_2 , and I_3) available at the acquired SPOT images:

$$ISI = a_0 + I_j + a_1 \cdot PC_1 + a_2 \cdot PC_2 + a_3 \cdot PC_3 + a_5 \cdot PC_5 \quad (4)$$

where a_i ($i = 1, 2, \dots, 5$) are the coefficients of principal components calculated from the four bands (B_1 , B_2 , B_3 , and B_4) of the SPOT data and Normalized Different Vegetation Index (NDVI) in Eq. 5 [14].

$$NDVI = (B3 - B2) / (B3 + B2) \quad (5)$$

In order to extract impervious surfaces areas, a threshold of ISI was chosen to extract impervious surface area within residential area. The remained area of the residential area was used as a garden class. Finally, land cover maps for 2003, 2007 and 2011 consisting of open water, vegetation, barren, impervious surfaces, and garden classes were constructed.

3.3 Markov Chain Model for Predicting Land Use Change

Markov chain model is a popular method used to predict temporal land use change [17]. In the Markov chain model, a stochastic process could be used to generate sequences of random variables [18] by probabilistic laws. The process is considered discrete in time, such as $T = 0, 4, 8 \dots$ years, which is considered a reasonable time interval for studying LULC change phenomenon. If the stochastic process follows a

Markov process then the sequence of random variables could be generated using the Markov property as in Eq. 6 below:

$$P[X_{n+1} = a_{in+1} | X_0 = a_{i0}, \dots, X_{in} = a_{in}] = P[X_{in+1} = a_{in+1} | X_{in} = a_{in}] \quad (6)$$

where the double index (*in*) means, and in this study, for $n \in T$ with $T = 0, 4, 8, \dots$ years; $i = 5$, a_i is the LULC class.

When the range of possible values for a_i is either finite or infinite denumerable, as in this study, the Markov process may be referred as a Markov chain. Therefore, one must prove that there is a statistical dependence between X_{n+1} and X_n (Eq. 7); and that statistical dependence is a first-order Markov process (Eq. 8).

$$P(X_n = a_n | X_{n-1} = a_{n-1}) \neq P(X_n = a_n) * P(X_{n-1} = a_{n-1}) \quad (7)$$

$$P[X_n = a_n | X_{n-1} = a_{n-1}] = P[X_n = a_n, X_{n-1} = a_{n-1}] / P[X_{n-1} = a_{n-1}] \quad (8)$$

A first-order Markov process is a Markov process where the transition from a class to any other does not require intermediate transitions to other states. The statistical dependence can be tested as in any contingency table [18] displaying the LULC change between X_n and X_{n-1} . In our study, this test was performed for the LULC change between 2007 and 2011. To infer from the association or independence between the LULC classes in different years from the contingency table, the random variable, with the chi-square distribution will be defined by Eq. 9:

$$\chi^2 = \sum_i \sum_j \frac{(O_{ij} - E_{ij})^2}{E_{ij}} \quad (9)$$

where O is the contingency matrix displaying the LULC change between 2007 and 2011, and E the contingency matrix with the expected values of change assuming the independence hypotheses [19]. χ^2 measures the distance between the observed values of LULC change and the expected ones assuming independence and must be high enough to prove Eq. 9, for 5° of freedom.

4 Results and Discussion

4.1 Landuse/Landcover Classification and Accuracy Assessment

For accuracy assessment of LULC map classified from the SPOT-5 images, the Land use map at scale of 1/10000 provided by COSAMD was used. 187, 276, 274 and 307 random pixels were chosen for four land cover classes consisting of open water, vegetation, barren and residential area, respectively. The summary of the accuracy assessment for LULC map in 2003, 2007 and 2011 was shown in Tables 2, 3, and 4, respectively. It was found that the accuracy of the open water class was the highest among the four land cover classes (both Producer's and User's accuracy were approximately 90%) because open water is very homogenous. However, the accuracy of residential area was lowest, this

Table 2. Accuracy assessment report of LULC map on 24/06/2003

Samples		Reference				Row total	Producer's accuracy
		Open water	Vegetation	Residential area	Barren		
Generated	Open water	171	9	0	7	187	0.91
	Vegetation	11	231	16	18	276	0.84
	Residential area	6	32	208	28	274	0.76
	Barren	2	8	45	252	307	0.82
Column total		190	280	269	305	1044	
User's accuracy		0.90	0.83	0.77	0.83		
Overall accuracy		0.83					
Kappa index		0.77					

Table 3. Accuracy assessment report of LULC map on 21/08/2007

Samples		Reference				Row total	Producer's accuracy
		Open water	Vegetation	Residential area	Barren		
Generated	Open water	172	8	0	7	187	0.92
	Vegetation	12	229	16	19	276	0.83
	Residential area	6	31	210	27	274	0.77
	Barren	2	9	46	250	307	0.81
Column total		192	277	272	303	1044	
User's accuracy		0.90	0.83	0.77	0.83		
Overall accuracy		0.82					
Kappa Index		0.76					

could be due to mixing between vegetation, barren and impervious surfaces (both Producer's and User's accuracy were approximately 76%).

Although, it is difficult to classify land cover classes of the urban area because of the mixing between vegetation, barren and impervious surfaces, and the conversion between land use depending on the time during the development period of city. The Kappa index of all land cover maps assessed was from 0.76 to 0.77. Meanwhile, the overall accuracy ranged from 0.82 to 0.83. These demonstrated the reliability of the classified maps.

Based on the LULC maps derived from object-oriented classification and ISI computed from SPOT-5 data of Hanoi area, final LULC maps for 2003, 2007 and 2011

Table 4. Accuracy assessment report of LULC map on 12/12/2011

Samples		Reference				Row total	Producer's accuracy
		Open water	Vegetation	Residential area	Barren		
Generated	Open water	173	8	0	6	187	0.93
	Vegetation	10	232	15	19	276	0.84
	Residential area	7	30	207	30	274	0.76
	Barren	3	8	43	253	307	0.82
Column total		193	278	265	308	1044	
User's accuracy		0.90	0.83	0.78	0.82		
Overall accuracy		0.83					
Kappa Index		0.77					

were established as shown in Fig. 4. Then the area of open water, vegetation, barren, impervious surfaces and garden were calculated and shown in Table 5. The changes of area by LULC classes were illustrated Fig. 5. It can be seen that the area of impervious surfaces increased dramatically from 6125.10 ha (21.30% of total area) in 2003 to 8426.88 ha (29.30% of total area) in 2007, and to 10525.21 ha (36.60% of total area) in 2011. Whereas, the area of vegetation decreased gradually from 10658.67 ha (37.07% of total area) to 9301.15 ha (32.34% of total area) in time period of 2003 to 2011. The same pattern can be seen for the area of garden reducing from 4760.47 ha in 2003 to 1964.33 ha in 2011. Meanwhile, area of barren and open water was almost steady. This indicated that vegetation and garden was mainly converted to impervious surface in the period of 2003 and 2011.

To generate map of change from four LULC classes (i.e. open water, vegetation, barren, and garden) to impervious surface, the LULC maps in 2003 and 2011 were superimposed by using ArcGIS software. The change of each class was represented by one different color for distinguishing one class among others classes as shown in Fig. 6.

Besides the visualization, the determination of land cover area changes from the land cover classes and impervious surfaces area between 2003 and 2011 was computed and shown in Table 6. From 2003 to 2011, the main changed area is from garden to impervious surfaces, which was changed about 3142.207 ha. This changed area was represented by red color area in Fig. 6. Besides, the vegetation and barren area transferred to vegetation area were about 882.47 ha and 340.19 ha, respectively.

According to Table 6 and Fig. 7, there was a lot changes among land cover classes from 2003 to 2011, but we only considered the increased area of impervious surfaces caused by changing from vegetation, open water, barren, and garden area. The percentage of change of vegetation, barren, open water, and garden area corresponding to the increased area of impervious surfaces was about 8.28% of total vegetation area, 10.27% of total barren area, 1.91% of total open water, and 66.01% of total garden area, respectively. This means that the change from garden area to impervious surfaces

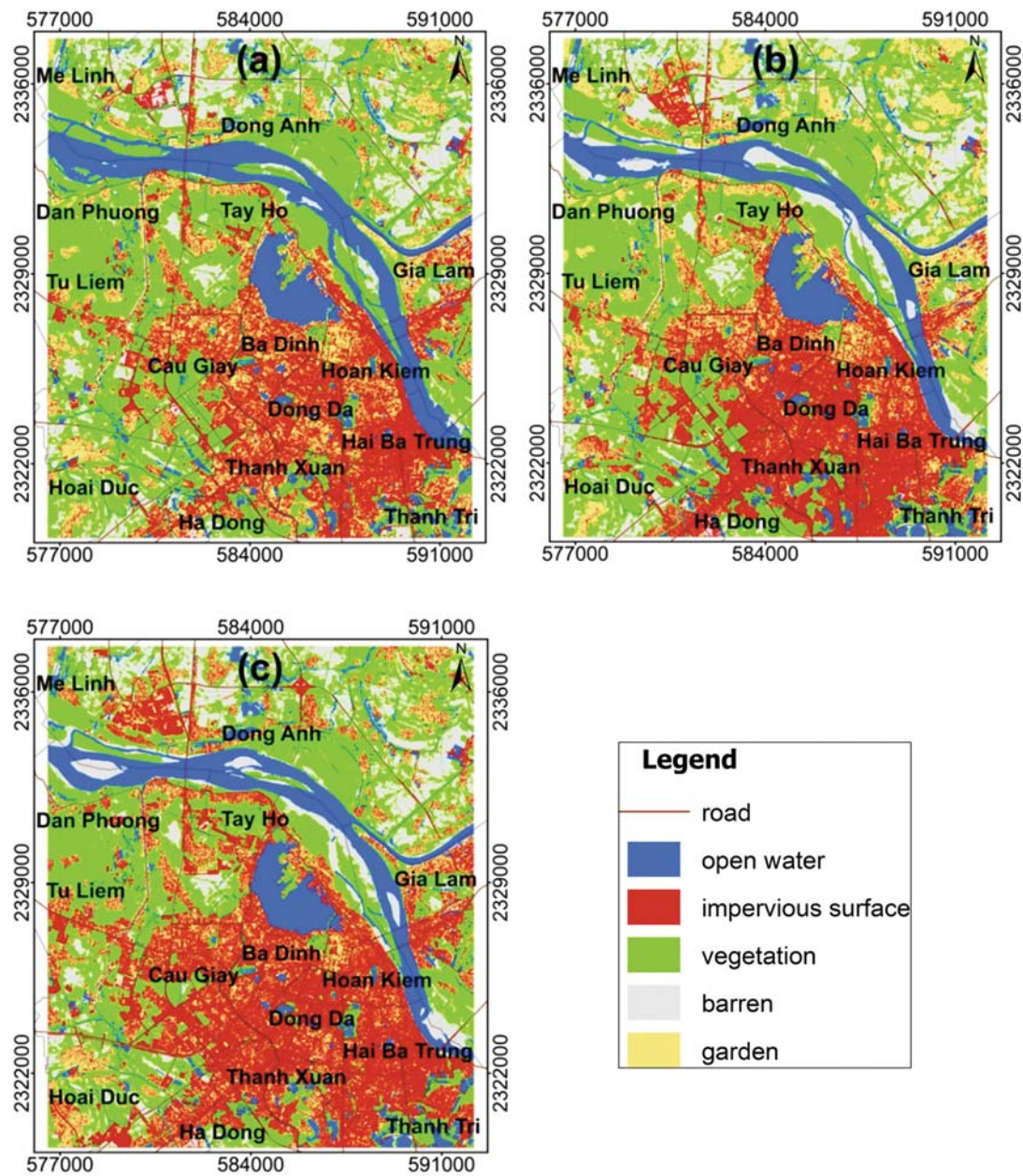


Fig. 4. LULC and impervious surfaces maps for different year: (a) year of 2003, (b) year of 2007, and (c) year of 2011

was dominant change for urbanization in Hanoi area. It may be explained that the policy of land use planning for urban in this period was the conversion of agricultural land to other land use classes.

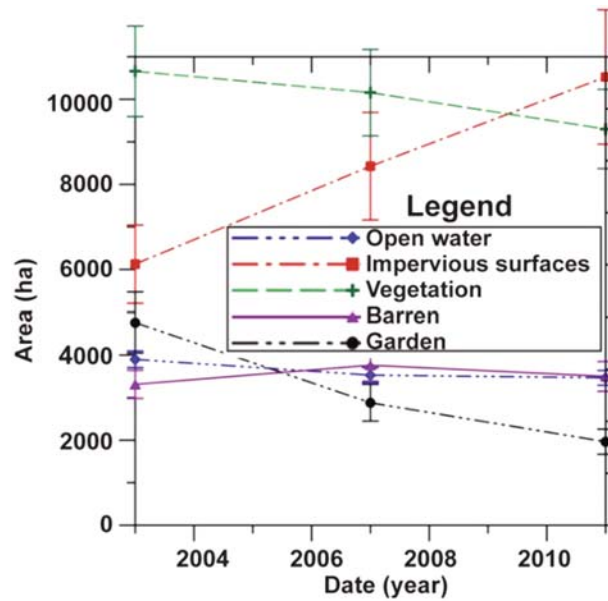
4.2 Prediction Based on Markov Chain Model

4.2.1 Modelling Results and Validation

In this study, the Markov model was performed using IDRISI Selva[®] software, version 17.0. To validate the model, the simulated LULC types need to be compared with

Table 5. LULC types and impervious surfaces area extracted from the SPOT data for the study area

Land cover	2003		2007		2011	
	ha	%	ha	%	ha	%
Open water	3899.77	13.56	3529.06	12.27	3465.95	12.05
Impervious surfaces	6125.10	21.30	8426.88	29.30	10525.21	36.60
Vegetation	10658.67	37.07	10157.38	35.32	9301.15	32.34
Barren	3312.35	11.52	3762.43	13.08	3499.72	12.17
Garden	4760.47	16.55	2880.61	10.02	1964.33	6.83
Total	28756.36	100	28756.36	100	28756.36	100

**Fig. 5.** LULC and impervious surfaces changes

actual area. Therefore, the simulated LULC types of 2011 generated from LULC maps in 2003 and 2007 with time step of 4 years was compared with the land use in 2011 classified from SPOT-5 image acquired in 2011. For this purpose, χ^2 test expressed as Eq. 10 was used in order to ensure suitability of the model. The test results were as follows (see Table 7):

$$\chi^2 = \sum \frac{(O - E)^2}{E} = 1.88 \quad (10)$$

According to Table 7, there was no significant difference between simulated value and actual value (1.88 is much smaller than 11.01). Therefore, Markov chain model can be used for predicting LULC types in Hanoi area.

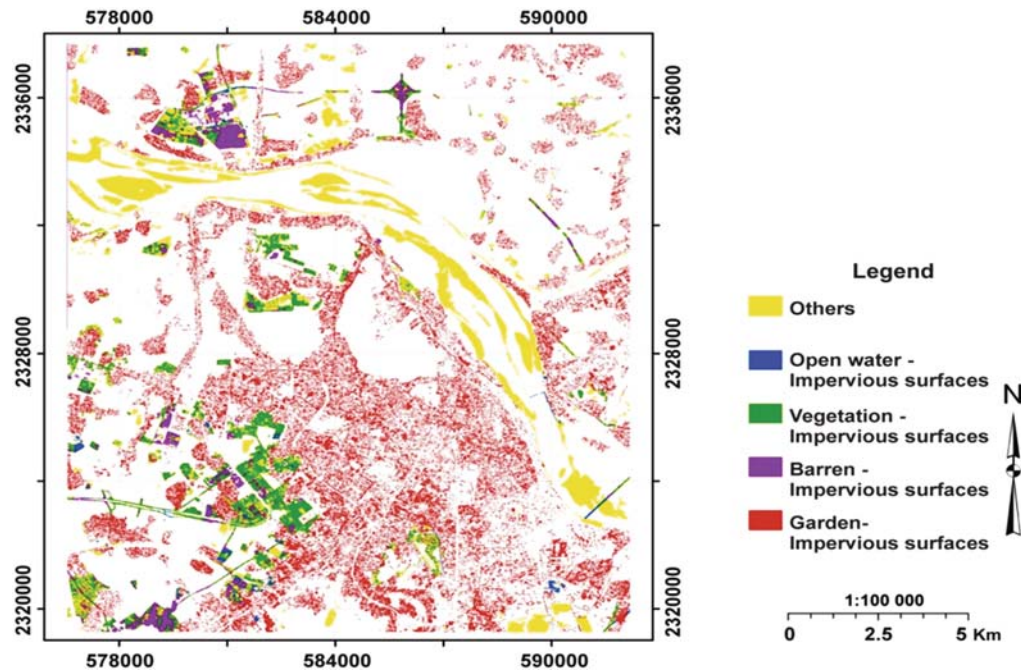


Fig. 6. Map of change from LULC to impervious surfaces between 2003 and 2011

Table 6. Change of LULC types to impervious surfaces between 2003 and 2011

2011	2003					
	Open water (ha)	Impervious surfaces (ha)	Vegetation (ha)	Barren (ha)	Garden (ha)	Total of 2003 (ha)
Open water	3180.82	74.59	49.39	583.02	11.95	3899.77
Impervious surfaces	15.96	6085.76	10.53	10.53	2.32	6125.10
Vegetation	171.07	882.47	9221.28	92.36	291.49	10658.67
Barren	91.07	340.19	7.97	2807.94	65.18	3312.35
Garden	7.03	3142.20	11.98	5.87	1593.39	4760.47
Total of 2011	3465.95	10525.21	9301.15	3499.72	1964.33	28756.36

4.2.2 Prediction of LULC Types in 2019 and 2027

Based on LULC maps in 2003 and 2011, the Markov chain model with time step of 8 years were used for predicting LULC types in 2019 and 2027. The results were shown in Table 8. According to Table 8, the increased area of impervious surfaces in 2019 and 2027 were about 8.27% and 14.09% of total study area, respectively due to the conversion from vegetation (4.09% and 7.64% of total study area, respectively) and open water (1.26% and 2.33% of total study area, respectively) and garden (3.22% and 4.46% of total study area, respectively). Besides, there was a little increase in area of barren could be due to loss of vegetation and open water caused by changing the

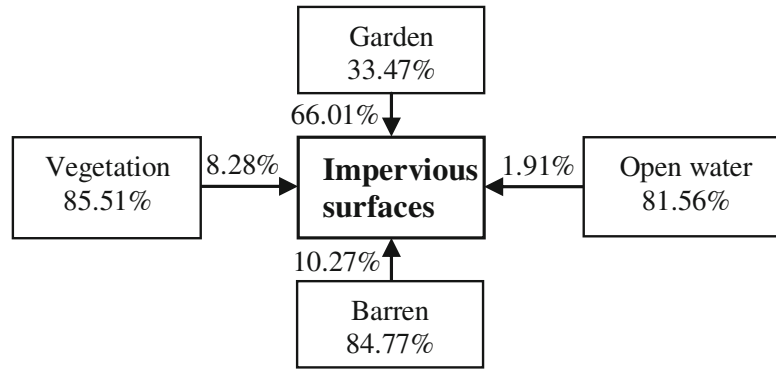


Fig. 7. Percentages of LULC transforming into impervious surfaces between 2003 and 2011

Table 7. Validation of LULC change forecast based on Markov chain model

LULC types	Chi-square test				
	Simulate value (O)	Actual value (E)	(O-E)	(O-E) ²	(O-E) ² /E
Open water	32.23	34.65	-2.42	5.87	0.17
Impervious surfaces	99.32	105.25	-5.93	35.18	0.33
Vegetation	96.82	93.01	3.81	14.56	0.15
Barren	41.16	34.99	6.17	38.08	1.09
Garden	18.01	19.64	-1.63	2.66	0.13
Total	287.56	287.56	0	96.37	1.88

Note: 5 degrees of freedom, χ^2 0.05 (5) = 11.01

Table 8. Trend of LULC changes simulated by Markov chain model in 2019 and 2027.

Year	LULC types					
	Open water (ha)	Impervious surfaces (ha)	Vegetation (ha)	Barren (ha)	Garden (ha)	Total (ha)
2003	3899.77	6125.10	10658.67	3312.35	4760.47	28756.36
2011	3465.95	10525.21	9301.15	3499.72	1964.33	28756.36
2019	3102.92	12902.69	8124.79	3586.95	1038.98	28756.36
2027	2795.15	14576.65	7103.02	3600.14	681.34	28756.36

purpose of land use. Those conversions among LULC types can be valuable information for the urban planning in Hanoi area.

5 Conclusion

In this study, the three SPOT images acquired in 2003, 2007 and 2011 were used to classify and extract the land cover classes consisting of vegetation, barren, open water, garden and impervious surfaces. The overall accuracy and Kappa index of all land

cover maps assessed were ranged from 0.76 to 0.77. Meanwhile, the overall accuracy ranged from 0.82 to 0.83. The impervious surfaces area has increased about 15.30% of total study area from 2003 to 2011 due to urban development. The main conversion was from garden to impervious surfaces area with the converted area was about 10.93% of total study area. The validation of the Markov chain model used to simulate LULC types in 2011 showed that Chi-square test was about 1.88 satisfied requirement of 5 degrees (χ^2 0.05 (5) = 11.01). Therefore, land cover maps in 2003 and 2011 were used to predict LULC types in 2019 and 2027 with time step of 8 years. The prediction indicated that there could be a significant expansion of impervious surfaces area in 2019 and 2027 with the expandable area of 8.27% and 14.09% of total study area, respectively. Those changes of LULC types revealed the trend of land use conversion, which may be caused by the policy of city administration.

References

1. Gregg, H., Angeles, L.: Globalization, industrialization and urbanization in pre-world War II Southeast Asia. *Explor. Econ. Hist.* **48**, 20–36 (2011)
2. Vu, M.H., Kawashima, H.: Effects of urban expansion on suburban farmers' livelihood in Vietnam: a comparative analysis of Ho Chi Minh City and Hanoi. *Habitat Int.* **65**, 49–58 (2017)
3. Hanoi Statistical Office: Hanoi Statistical Yearbook. Statistics Publishing House (2003, 2007 and 2011)
4. Park, S., Jeon, S., Kim, S., Choi, C.: Prediction and comparison of urban growth by land suitability index mapping using GIS and RS in South Korea. *Landscape Urban Plan.* **99**, 104–114 (2011)
5. Jat, M.K., Choudhary, M., Saxena, A.: Urban growth assessment and prediction using RS, GIS and SLEUTH model for a heterogeneous urban fringe. *Egypt. J. Remote Sens. Space Sci.* (2017). In Press, Corrected Proof
6. Muller, M.R., Middleton, J.: A Markov model of land-use change dynamics in the Niagara Region, Ontario. *Can. Landscape Ecol.* **9**, 151–157 (1994)
7. Yang, X., Zheng, X.Q., Lv, L.N.: A spatiotemporal model of land use change based on ant colony optimization, Markov chain and cellular automata. *Ecol. Model.* **233**, 11–19 (2012)
8. Hanoi Statistical Office: General inventory results of the census, economic, administrative and professional establishments (2007)
9. Chen, W.T., Zhang, Z., Wang, Y.X., Wen, X.P.: Atmospheric Correction of SPOT5 land surface imagery. In: 2nd International Congress on Image and Signal Processing. IEEE, Tianjin (2009)
10. Trimble: eCognition Developer 8.7: User Guide. Trimble Germany GmbH, Trappentreustr. 1, D-80339 München, Germany (2011)
11. Willhauck, G., Schneider, T., De Kok, R., Ammer, U.: Comparison of object-oriented classification techniques and standard image analysis for the use of change detection between SPOT multispectral satellite images and aerial photos. In: XIX ISPRS Congress (2000)
12. Manakos, I.: eCognition and Precision Farming. eCognition Application Notes 2, (2001)

13. Mitri, G.H., Gitas, I.Z.: The development of an object-oriented classification model for operational burned area mapping on the Mediterranean island of Thasos using LANDSAT TM images. In: Viegas, D.X. (ed.) *Forest Fire Research & Wildland Fire Safety*. Millpres, Rotterdam (2002)
14. Pairman, D., McNeill, S., Belliss, S.: *Impervious surface mapping for the auckland region*. Prepared by Landcare Research for Auckland Regional Council (2010)
15. Huete, A., Justice, C., Liu, H.: Development of vegetation and soil indexes for MODIS-EOS. *Remote Sens. Environ.* **49**, 224–234 (1994)
16. Hanqiu, X.: Modification of normalized difference water index(NDWI) to enhance open water feature in remotely sensed imagery. *Int. J. Remote Sens.* **27**, 3025–3033 (2006)
17. Zheng, H.W., Shen, G.Q., Wang, H., Hong, J.: Simulating land use change in urban renewal areas: A case study in Hong Kong. *Habitat Int.* **46**, 23–34 (2015)
18. Murteira, B.: *Probabilidades e estatística*. McGraw-Hill Portugal (1990)
19. Cabral, P., Zamyatin, A.: Markov processes in modeling land use and land cover changes in Sintra-Cascais, Portugal. *DYNA* **76**, 191–198 (2009)